

Journal of Materials Chemistry C

Accepted Manuscript



This is an *Accepted Manuscript*, which has been through the Royal Society of Chemistry peer review process and has been accepted for publication.

Accepted Manuscripts are published online shortly after acceptance, before technical editing, formatting and proof reading. Using this free service, authors can make their results available to the community, in citable form, before we publish the edited article. We will replace this *Accepted Manuscript* with the edited and formatted *Advance Article* as soon as it is available.

You can find more information about *Accepted Manuscripts* in the [Information for Authors](#).

Please note that technical editing may introduce minor changes to the text and/or graphics, which may alter content. The journal's standard [Terms & Conditions](#) and the [Ethical guidelines](#) still apply. In no event shall the Royal Society of Chemistry be held responsible for any errors or omissions in this *Accepted Manuscript* or any consequences arising from the use of any information it contains.

Probing the doping mechanisms and electrical properties of Al, Ga and In doped ZnO prepared by spray pyrolysis

Robert Maller¹, Yoann Porte¹, Husam N. Alshareef² and Martyn A. McLachlan^{1*}

1. Department of Materials and Centre for Plastic Electronics, Imperial College London, London SW7 2AZ, United Kingdom

2. Materials Science and Engineering, King Abdullah University of Science and Technology (KAUST), Thuwal 23955-6900, Saudi Arabia

*martyn.mclachlan@imperial.ac.uk

Abstract

The measured structural, optical and electrical properties of Al, Ga and In doped ZnO films deposited using spray pyrolysis are reported over the doping range 0.1 - 3 at%. Over the entire doping series highly transparent, polycrystalline thin films are prepared. Using AC Hall as a measurement technique we probe the electronic properties of our doped films, deconvoluting the impact of doping on the measured charge carrier concentrations and Hall mobility. We focus on the low doping range *i.e.* 0.1 - 1 at%, where we observe unexpected variations in charge carrier concentration and mobility and propose a mechanism to explain our observations. In this doping range highly resistive films are formed hence we highlight AC Hall as a reliable and highly reproducible technique for analysing electrical properties and subsequently elucidate the doping mechanisms. The implementation of a simple, post-deposition heat treatment demonstrated on our AZO results in typical films with charge carrier concentrations exceeding $> 10^{19} \text{ cm}^{-3}$, and electron mobilities $> 10 \text{ cm}^2/\text{Vs}$ and stability exceeding 180 days. We describe in detail the nature of the defect chemistry and the role of intrinsic defects and show, that despite significant variations in dopant species and grain boundary concentrations, that the defect chemistry dominates the electrical characteristics.

Introduction

Interest in transparent conducting oxides (TCOs) has intensified over the past decade as the search for a suitable replacement for indium tin oxide (ITO) continues. This has been driven by escalating indium costs, energy intensive manufacturing requirements for ITO¹ and concerns over release of indium and oxygen into active

layers, particularly of organic devices.² Numerous candidates have been identified as transparent electrodes ranging from polymeric systems,³ carbon nanotubes,⁴ graphene,⁵ metallic nanostructures⁶ and doped metal oxides.⁷ Of these candidates, doped metal oxides are of particular interest owing to their ease of fabrication, suitability for large area processing, low-cost and tuneable electronic properties.

Zinc oxide (ZnO) has been the prototypical oxide for many investigations as fabrication can be achieved using a wide range of accessible techniques, often with little capital investment and using ubiquitous precursor materials. ZnO has been studied for many decades owing to its n-type conductivity, wide band gap, excellent charge carrier mobility and ease of processing.⁸⁻¹² The conductivity of ZnO is considered to arise from a variety of native point defects including; oxygen vacancies (V_O), zinc interstitials (Zn_i), zinc anti-sites and more recently to the incorporation of interstitial hydrogen.¹³ The charge carrier mobility and concentration in ZnO can be further enhanced by the inclusion of dopant atoms, typically group III elements^{14,15} or by the creation of intrinsic defects via thermal treatments under vacuum, argon or hydrogen environments.¹⁶

For the thermal treatments several mechanisms have been proposed, namely the creation of V_O ¹⁷ which act as point defects contributing two electrons to the conduction band. However such defects are considered deep donors - hence this mechanism is unlikely, particularly in the bulk.¹⁸ It has therefore been suggested that thermal treatments lead to desorption of oxygen acceptor states at the surface or at grain boundaries, which act as electron traps to lower charge mobility.¹⁹ Finally annealing in hydrogen or partial vacuum may facilitate hydrogen doping, where hydrogen acts exclusively as a shallow donor.¹³ Indeed one or all of these defect species may contribute to the enhanced conductivity of ZnO post anneal. Given the nature of the deposition techniques used it is likely that in those reliant on vacuum *e.g.* chemical vapour deposition (CVD), pulsed laser deposition (PLD) or sputtering,²⁰⁻²² such defects may be inherent whereas solution based deposition methods *e.g.* spin-coating, sol-gel, and spray pyrolysis¹⁶ may require post deposition thermal treatments. The development of modified deposition techniques *e.g.* aerosol assisted CVD²³⁻²⁵ or low temperature PLD^{26,27,14} have had substantial impact with regards to controlling film growth, defect chemistry and electronic properties of the ZnO system.

Considering the group III dopants, specifically Al, Ga and In, 3^+ cations are proposed to substitute Zn in the lattice and donate one additional electron to the conduction

band thus increasing the free carrier concentration. In physical deposition methods dopants can be readily combined into targets and for solution deposition routes they can be simply included into precursor mixtures. This has been widely studied as a means to increase the free carrier concentration and lower resistivity.^{17,28,29} Recently there has been a renewed interest in ZnO and doped ZnO as an electron transporting/hole-blocking layer in organic solar cells^{28,30} ^{24, 26} and organic light emitting diodes³¹ further highlighting the applicability of these materials beyond TCO applications.

Of the many deposition methods studied spray pyrolysis (SP) offers a convenient route to the growth of controlled composition, large-area thin films in ambient conditions^{32,33}. Doping of oxide semiconductors using SP has been well studied as a means of enhancing free carrier mobility and increasing conductivity.^{12,16,32,34} With particular reference to group III dopants in ZnO numerous reports have been made^{17,35,36}, the general observation is that above an optimum doping level performance degrades. Advances in the SP technique have produced improved results via modifications in precursor composition,³⁷ the use of ultrasonic nozzles^{38,39} and by depositing in low humidity, oxygen deficient environments.⁴⁰ Using AC Hall effect measurements changes in the electrical properties have been separated into contributions from carrier mobility and carrier concentration.³⁸ However owing to the often high resistivity of undoped ZnO and ZnO prepared at low doping levels it has been challenging to study such a wide range of doping levels of such thin films using one technique. Here we show the influence of Al, Ga and In doped ZnO (AZO, GZO, IZO respectively) on charge carrier mobility/concentration and film resistivity over the doping range 0 - 3 at%, with a specific emphasis on the behaviour between 0 - 1 at%. A mechanism is proposed for the observed electronic behaviour of as-deposited group III doped thin films and their behaviour following various thermal treatments. To the best of the author's knowledge these properties are to-date unreported in films deposited by SP.

Experimental

All films were deposited on glass substrates using a custom automated pneumatic spray pyrolysis system. 1 x 1 cm glass substrates were ultrasonically cleaned in deionised water, acetone then isopropanol for 5 minutes before being nitrogen blow-dried. All precursors were purchased from Sigma Aldrich and used as received. Zinc acetate dihydrate ($\text{Zn}(\text{CH}_3\text{COO})_2 \cdot 2\text{H}_2\text{O}$, $\geq 99\%$) was dissolved in methanol and

acetic acid at a volume ratio of 95:5 to prepare 0.1 mol dm⁻³ solutions. In separate flasks aluminium chloride hexahydrate (AlCl₃.6H₂O, ≥99%), gallium nitrate hydrate (Ga(NO₃)₃.xH₂O, 99.9%) and indium nitrate hydrate (In(NO₃)₃.xH₂O, 99.9%) were also prepared to 0.1 mol dm⁻³ solutions in the same solvent. The zinc and dopant salts were kept separate until immediately prior to deposition to avoid any precipitation that was occasionally observed in aged solutions - particularly when using indium nitrate hydrate. The substrates were placed onto a hotplate and preheated to 400 °C and the precursor solutions mixed to achieve the desired composition. Films were sprayed to a constant thickness of 150 nm doped with 0, 0.1, 0.2, 0.3, 0.4, 0.5, 1, 2 and 3 at% of Al, Ga and In. The quoted doping levels used throughout refer to the loading of dopant in the precursor solutions. Compressed air was used as a carrier gas with a spray rate of 10 ml/min. Regular pauses to the deposition were used to allow the substrate to return to the set temperature. Post deposition annealing was performed on AZO samples at 500 °C for one hour in Ar and O₂ (in separate anneals), following initial measurements. The resulting films were measured using XRD (PANalytical), UV-Vis (Bentham 605 single beam system), High-resolution TEM imaging was carried out on cross-sections prepared using an FEI Helios dual beam instrument and imaged in bright field mode at 200 kV (JEOL JEM-2100). Hall effect measurements were obtained using films on glass substrates with indium contacts deposited in the van der Pauw geometry (Lakeshore 8404 in AC field mode, current 10 nA - 50 mA under a field of 1.19 T). SEM images were obtained after coating samples with a thin Cr to ensure good conductivity at a typical accelerating voltage of 5 -10 kV.

Results and Discussion

The UV-Vis transmittance measurements, **Figure S1**, confirm high optical transparencies $< 85\%$ over the visible range with consistent measured film thicknesses of ~ 150 nm. The optical bandgap of all films were obtained via Tauc analysis were in the range of 3.25 ± 0.03 eV with no systematic variation observed with dopant type or concentration, **Figure S2**. The X-ray diffraction (XRD) data for all films prepared are shown in **Figures 1 a - d**, confirming the deposition of polycrystalline wurtzite ZnO. Analysis of the XRD data and the texture coefficients calculated for all films confirm a strong preferential (002) preferred orientation for all dopants species at all concentrations, **Figure 2a**. There is a drop in the degree of preferred (002) orientation from 0 - 0.5 at%, over which range there is a corresponding increase in the preferred (103) orientation (**Table S1**). Extremely small variations in the (002) peak position are observed as the dopant species and concentration are varied, indicating changes in the $d_{(002)}$ lattice spacing of < 0.1 Å. Over the doping range investigated both GZO and IZO show only slight decreases in $d_{(002)}$ compared with ZnO. In contrast the $d_{(002)}$ spacing for AZO falls more dramatically until 1 at%. These trends may be attributed to the Al having a significantly smaller cation size than Zn^{2+} whilst Ga and In are much more similar ionic radii.⁴¹ The ionic radii for divalent and trivalent cations in 4-coordinate systems $\text{Zn}^{2+} = 0.60$ Å, $\text{Al}^{3+} = 0.39$ Å, $\text{Ga}^{3+} = 0.47$ Å, $\text{In}^{3+} = 0.62$ Å. This leads to a larger decrease in lattice size when the Al substitutes into the Zn lattice position. The XRD data show no evidence of secondary phases present for any of the dopant species investigated over the entire concentration range. In parallel, there is change in the measured full-width at half-maximum (FWHM) of the (002) diffraction peak. Such broadening can be influenced by changes to the crystallite size calculated using Scherrer analysis **Figure 2b**. The crystallite size is seen to decrease at high dopant level in AZO and IZO films but GZO remains stable with the undoped ZnO. Typical SEM micrographs confirm this observation, **Figure 3**, showing undoped thin films of ZnO alongside 0.2 and 2 at% AZO, GZO and IZO. At 0.2 at% doping the grains of the AZO films show no appreciable change in size or shape compared with ZnO, however both GZO and IZO appear to have a reduced grain size *i.e.* an increased concentration of grain boundaries. When doping is increased to 2 at% both AZO and IZO films appear to be comprised of much smaller grains than the undoped ZnO however the grain size of GZO remains similar to that observed at 0.2 at%. Changes in the surface morphology for AZO are observed, which may be consistent with the subtly reduced (002) peak intensity in the XRD data. From the SEM and XRD

analysis we can conclude that the variation in crystallite size (XRD) or grain size/morphology (SEM) is having no influence on the measured electrical properties (see below). This is anticipated as the crystallite size is significantly larger than the mean free path of our charge carriers, typically a few nm⁴², and at high carrier concentrations changes in the levels of ionised impurity scattering will dominate the charge transport⁴³. There is however a change in carrier concentration and charge mobility consistent with the observed changes in preferential orientation at low doping concentrations. In some films the presence of metallic indium is observed in XRD patterns deriving from the contacts used in AC Hall Effect measurements. The peak seen at $\sim 32^\circ 2\theta$ is a close match with the (100) ZnO orientation however the exact position and FWHM of the peak confirm the presence of metallic indium, present as a contact material for AC Hall measurement.

The measured carrier concentration, AC Hall mobility and resistivity values for the AZO, GZO and IZO films prepared are shown in **Figure 4**. With all dopants, the addition of 0.1 at% results in a sharp rise in free carriers, from $3.65 \times 10^{16} \text{ cm}^{-3}$ in ZnO to $8.84 \times 10^{17} \text{ cm}^{-3}$, $2.28 \times 10^{18} \text{ cm}^{-3}$ and $2.55 \times 10^{17} \text{ cm}^{-3}$ for AZO, GZO and IZO respectively. The increase in carrier concentration saturates at different dopant concentrations for all 3 systems, specifically: 0.2 at% for AZO ($5.61 \times 10^{18} \text{ cm}^{-3}$), 0.5 at% for GZO ($1.24 \times 10^{19} \text{ cm}^{-3}$) and 1 at% for IZO ($2.08 \times 10^{19} \text{ cm}^{-3}$). After saturation little variation in carrier concentration is observed. In contrast the charge carrier mobility falls sharply on the addition of all dopants. In AZO carrier mobility begins to increase above 0.1 at% doping, whereas in GZO and IZO the rise occurs above 0.5 at%. In AZO and IZO the carrier mobility of undoped ZnO is eventually recovered but in the GZO the measured carrier mobility for all dopant concentrations never returns to that of pure ZnO. When comparing carrier concentration and mobility it appears that the carrier mobility mirrors the carrier concentration data suggesting a correlation between the two parameters. As a result of the variation in the carrier concentration and mobility significant changes in film resistivity are seen across the entire doping series, where doping to 0.5 at% results in a near 2 orders of magnitude reduction in resistivity from the undoped ZnO (3000 $\Omega\cdot\text{cm}$), **Figure 4b**. Above 0.5 at% the AZO and GZO films continue to fall reaching their minimum values (1 at%, 13.6 $\Omega\cdot\text{cm}$ – AZO), (3 at%, 65.6 $\Omega\cdot\text{cm}$ - GZO). The IZO film resistivity continues to fall sharply until a doping concentration of 1 at% whereupon it stabilises, reaching a minimum value of 5.2 $\Omega\cdot\text{cm}$ at 3 at%. Above 3 at% doping, resistivity is expected to increase.³² It should be noted that in such well-studied systems there is a relationship between film thickness and the measured electrical properties, see supplemental **tables 1-3**. Here

were maintain film thickness at around 150 nm, which allows the comparative characterisation to be obtained, the film properties measured are consistent with films of comparable thickness reported in the literature.

Doping may also occur non-substitutionally – as charged species in interstitial sites, in secondary phases comprised of their native oxides (usually migrating to grain boundaries) or in zinc-dopant complex systems, also usually found at grain boundaries,⁴⁴ or through non-donor substitution. At such low doping concentrations secondary phases are likely to be beyond the detection limit of XRD so to measure the formation of such secondary phases at grain boundaries Energy Dispersive X-Ray spectroscopy (EDX) was carried out on AZO in the transmission electron microscope (TEM). **Figure 5a** shows a typical dark field micrograph for 2 at% AZO in which a number of individual grains and boundaries can be clearly identified. At this dopant level the AC Hall measurements show that the charge carrier concentration and mobility have stabilised, thus it is anticipated that grain boundary accumulation of the dopant should be quantifiable if this mechanism is occurring. EDX line scans across multiple grain boundaries, an example of which is shown in **Figure 4b**, show no evidence of Al accumulation and confirm the homogeneous distribution of the dopant across the specimen. The TEM analysis gives the third independent measure of grain size in the films, with grains in the size range 30 – 50 nm observed, which compares well with the calculated $d_{(002)}$ from XRD of 20 – 35 nm. Both TEM and XRD are probing the grain size through the thickness of the film whilst the SEM analysis is imaging the grain structure laterally, for which the measured grain size is larger, typically 30-80 nm.

The combined variation in measured electrical behaviour can be described by considering the processes that may be occurring on doping. Initially the sharp rise in carrier concentration is attributed to the increase in donor species; this reduces carrier mobility but drives an overall reduction in resistivity. The initial reduction mobility is believed to be caused by an the combined effect of *i*) an increase in ionised impurity scattering or, *ii*) increased charge-charge and charge-phonon interactions, carrier concentration increases⁴⁵ and changes in the orientation of the films. Beyond a critical point dopant ions cease to donate electrons to the conduction band and the measured carrier concentration saturates. This occurs at different concentrations for each of the dopant species investigated. The continued decrease in lattice spacing beyond the saturation point, measured from our XRD analysis, suggests that dopants are not filling interstitial sites and TEM analysis, coupled with

the sustained drop in resistivity, imply that the formation of insulating secondary phases e.g. Al_2O_3 or ZnAl_2O_4 are unlikely. One theory is that the field created by ionised dopants prohibits additional charged species from locating in near proximity, as such the dopants are forced into neutral, non-carrier donating, substitutional states.⁴⁶ Considering the low at% at which the saturation occurs this also seems an unlikely mechanism.

Our theory is that the ambient deposition conditions create an oxygen rich environment. As discussed, V_o are not considered to be a likely cause of n-type conductivity in ZnO as they are deep donors. Furthermore under these conditions the formation energy of Zn_i and V_o donor defects are increased, thus such defects become less prevalent. This is consistent with the observed lower carrier concentrations measured in SP deposited films compared with zinc rich environments of well-studied vacuum techniques such as PLD and magnetron sputtering - where carrier concentrations in the order of 10^{21} cm^{-3} are reported.^{47,48}

As the Fermi energy rises with increasing free carrier concentration⁴⁹, the formation energy of a dopant occupying a substitutional site increases. In parallel, the formation energy of an $\text{Al}_{\text{Zn}}\text{V}_{\text{Zn}}$ acceptor hybrid defect decreases and, in oxygen rich conditions, falls below that of the Al_{Zn} .⁵⁰ $\text{Al}_{\text{Zn}}\text{V}_{\text{Zn}}$ formation competes with Al_{Zn} formation and compensates for further added carriers thus charge carrier saturation is observed. This hybrid defect state also converts a doubly accepting, low formation energy, V_{Zn} state to the singly accepting hybrid therefore partially passivating the V_{Zn} trap. The onset of formation of $\text{Al}_{\text{Zn}}\text{V}_{\text{Zn}}$ would account for the increase in mobility seen in the films after the initial doping. It is believed that a similar mechanism would occur in GZO and IZO. The mobility is seen to plateau above 1 at% in AZO, combined with a slight increase in resistivity (**Figure 4**). We believe that above 1 at% Al no longer dopes substitutionally instead moving to the various sites mentioned earlier, or perhaps migrating to grain boundaries at concentrations lower than our EDX detection limit. In GZO and IZO films the difference in ionic size between Zn and the dopant is less allowing greater solubility in substitutional positions. This is supported by the smaller decreases seen in lattice size.

To investigate the hypothesis that mobility and carrier concentration are controlled by the fluctuating levels of Al_{Zn} , V_{Zn} and $\text{Al}_{\text{Zn}}\text{V}_{\text{Zn}}$ defect states a series of post deposition thermal anneals were performed. Al doping was used to highlight our hypothesis where a series of AZO films sequentially annealed in Ar, O_2 and Ar environments.

Between each anneal the electrical properties were studied with the results summarised in **Figure 6**. Following the first Ar anneal the carrier concentration and the mobility of the doped films both increase. The increase is more pronounced when dopants are added in contrast to the undoped ZnO control – at 1 at% mobility and carrier concentration are seen to increase by six and fourfold respectively. This is consistent with our hypothesis – that annealing in Ar shifts the system to a zinc rich (oxygen deficient) regime. This will increase the formation energy of V_{Zn} and thus the $Al_{Zn}V_{Zn}$ hybrid defects. Reducing the carrier compensating V_{Zn} and $Al_{Zn}V_{Zn}$ traps would account for the increased mobility seen in the system whilst the increased formation energy of the hybrid defect would lead to a higher proportion of Al_{Zn} donor defects thus accounting for the increased carrier concentration. A second anneal, this time in O_2 , significantly reduces the carrier concentration with little impact on the carrier mobility. Again this is consistent with our hypothesis – here an oxygen rich environment is created resulting in V_{Zn} and $Al_{Zn}V_{Zn}$ defects dominating. These act as charge trapping states thus the annealing treatment does not contribute to an improvement in charge mobility. After a final anneal in Ar the system is shifted to a zinc rich regime and both carrier concentration and mobility are increased. Here it is seen that at 1 at% the carrier concentration exceeds 10^{19} cm^{-3} and carrier mobility exceeds $10 \text{ cm}^2/\text{Vs}$. Interestingly, there is no variation in intensity or position of the (002) reflection from XRD data **Figure S3** following annealing treatments, this indicates that the observed improvements are not attributed to improvements in crystallinity or increase in crystallite size. **Figure 7** shows that improvements to the electrical properties are inherently stable following our annealing cycle, with measured resistivity, carrier concentration and mobility for ZnO/AZO stored in ambient air for 180 days shown.

Conclusions

Here we have demonstrated ambient spray pyrolysis as a convenient method for the formation of group III doped ZnO thin films. Combining X-ray diffraction and AC field Hall Effect measurements we propose a mechanism for the observed variation in Hall mobility, carrier concentration and film resistivity as the dopant species and concentration are varied. The study reveals that free carrier saturation occurs at a lower dopant level than previously reported ($< 0.2 \text{ at\%}$ in AZO). Maximum carrier concentrations are found at different doping levels with Al, Ga and In which we ascribe to dopants being incorporated as substitutional species and the efficiency of this process being determined by the dopant cation size. In the as deposited films we

show significant enhancements in charge carrier concentrations but in parallel a reduction in charge carrier mobility. We explain this observation by considering ionic defect scattering and orientation changes in the polycrystalline films – we specifically rule our grain boundary scattering as a significant contributing factor. The increase in mobility observed after carrier concentration saturation is explained by considering to the formation of $Al_{Zn}V_{Zn}$ acceptor defect states. Whilst we note that our measured values of carrier concentration, carrier mobility and film resistivity may be in general appear inferior to other published reports. To explain this and emphasise the significance of our results we highlight technologically relevant thicknesses and optical transparencies of our films combined with a measurement of electrical properties that is carried out in the dark and in the absence of any gate field – which may have a detrimental impact on measured properties. Our study is a rigorous, consistent investigation carried out over a wide doping concentration using multiple dopant species with a consistent electrical measurement technique used throughout and the data generated compares favourably with other literature reports for comparable doped-ZnO thin films (**Tables S2-4**). Through simple post deposition thermal treatments we show that charge carrier concentration and, in parallel the charge mobility, can be increased significantly, this consistent with our proposed mechanisms. The inherent scalability and low cost of ambient spray pyrolysis combined with the facile nature of compositional variation highlight the potential of this process for integration into large area optoelectronic platforms.

Acknowledgements

The authors gratefully acknowledge the KAUST-Imperial College Academic Excellence Alliance for financial support. The authors thank Dr D Payne (Imperial) for useful discussions in revision of the manuscript.

Figure Captions

Figure 1 XRD data obtained from ZnO films doped with 0 – 3 at % a) aluminium (AZO), b) gallium (GZO), and c) indium (IZO). In all cases the wurtzite structure is adopted. Note samples were measured following Hall analysis and show the presence of metallic indium indicated *.

Figure 2 – a) calculated texture coefficient (002) for AZO, GZO and IZO thin films, a clear change in orientation at low-doping concentrations is observed, b) shows the crystallite size of obtained from the (002) diffraction peak for the same films (colours as Figure 2a).

Figure 3 – SEM micrographs showing surface morphology of a range of thin films a) undoped ZnO (x 3), b) 0.2 at% AZO, c) 2 at% AZO, d) 0.2 at% GZO, e) 2 at% GZO, f) 0.2 at% IZO, g) 2 at% IZO (all scale bars 1 μ m).

Figure 4 – Measured electrical characteristics obtained from AC-Hall measurements, a) Hall mobility (blue) and charge carrier concentration (red) of 0 - 3 at% AZO, b) 0 - 3 at% GZO, c) 0 - 3 at% IZO, d) shows the calculated resistivity values for all films.

Figure 5 – TEM analysis of 2 at% AZO films, a) Dark field image of AZO cross section in STEM mode, the inset box highlights the beam-damaged region where EDX analysis was obtained, b) line scan data obtained across grain boundary highlighted in Figure 5a with data tabulated in Figure 5c below, d) HR-TEM images showing several crystal domains from which the lattice spacings are labelled – these values are consistent with data obtained by XRD analysis (2 at% AZO) summarised in insert table.

Figure 6 – Charge carrier mobility and concentration (a-d) and film resistivity (e-h) for as prepared AZO series (a + e); following an anneal in argon (b + f); following a subsequent anneal in oxygen (c + g) and following a final anneal in argon (d + h).

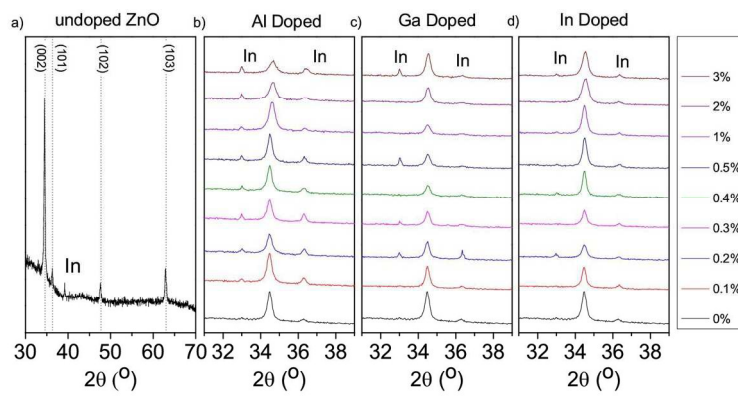
Figure 7 – a) Stability of resistivity, and b) mobility/ carrier concentration enhancements of 2 at% AZO film treated by the thermal annealing route outlined.

References

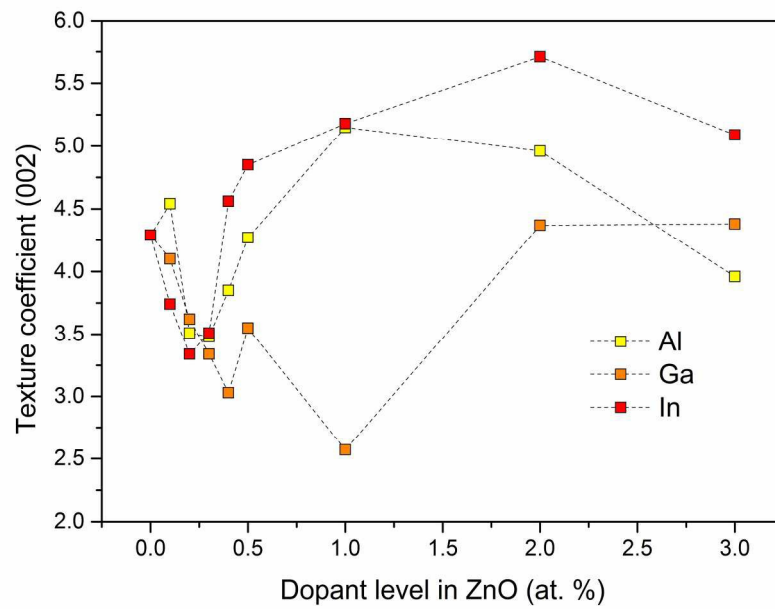
- 1 C. J. M. Emmott, A. Urbina and J. Nelson, *Sol. Energy Mater. Sol. Cells*, 2012, **97**, 14–21.
- 2 D. Alemu, H.-Y. Wei, K.-C. Ho and C.-W. Chu, *Energy Environ. Sci.*, 2012, **5**, 9662.
- 3 D. A. Mengistie, M. A. Ibrahim, P.-C. Wang and C.-W. Chu, *ACS Appl. Mater. Interfaces*, 2014, **6**, 2292–9.
- 4 J. van de Lagemaat, T. M. Barnes, G. Rumbles, S. E. Shaheen, T. J. Coutts, C. Weeks, I. Levitsky, J. Peltola and P. Glatkowski, *Appl. Phys. Lett.*, 2006, **88**, 233503.
- 5 J. K. Wassei and R. B. Kaner, *Mater. Today*, 2010, **13**, 52–59.
- 6 L. Hu, H. S. Kim, J.-Y. Lee, P. Peumans and Y. Cui, *ACS Nano*, 2010, **4**, 2955–63.
- 7 T. Schneller, H. Kohlstedt, A. Petraru, R. Waser, J. Guo, J. Denlinger, T. Learmonth, P. A. Glans and K. E. Smith, *J. Sol-Gel Sci. Technol.*, 2008, **48**, 239–252.
- 8 D. C. Look, D. C. Reynolds, J. R. Sizelove, R. L. Jones, C. W. Litton, G. Cantwell and W. C. Harsch, *Solid State Commun.*, 1998, **105**, 399–401.
- 9 Ü. Özgür, Ya. I. Alivov, C. Liu, A. Teke, M. A. Reshchikov, S. Doan, V. Avrutin, S.-J. Cho, H. Morkoç, Ü. Özgür, Y. Alivov, C. Liu and A. Teke, *J. Appl. Phys.*, 2005, **98**, 41301.
- 10 M. H. Weber, F. A. Selim, D. Solodovnikov and K. G. Lynn, *Appl. Surf. Sci.*, 2008, **255**, 68–70.
- 11 E. M. C. Fortunato, P. M. C. Barquinha, A. C. M. B. G. Pimentel, A. M. F. Gonçalves, A. J. S. Marques, R. F. P. Martins and L. M. N. Pereira, *Appl. Phys. Lett.*, 2004, **85**, 2541.
- 12 A. Bashir, P. H. Wöbkenberg, J. Smith, J. M. Ball, G. Adamopoulos, D. D. C. Bradley and T. D. Anthopoulos, *Adv. Mater.*, 2009, **21**, 2226–2231.
- 13 C. G. Van de Walle, *Phys. Rev. Lett.*, 2000, **85**, 1012–1015.
- 14 J. B. Franklin, J. B. Gilchrist, J. M. Downing, K. A. Roy and M. A. McLachlan, *J. Mater. Chem. C*, 2014, 84–89.
- 15 K. Zilberberg, J. Meyer and T. Riedl, *J. Mater. Chem. C*, 2013, **1**, 4796–4815.
- 16 A. F. Aktaruzzaman, G. L. Sharma and L. K. Malhotra, *Thin Solid Films*, 1991, **198**, 67–74.
- 17 H. Hung-Chun Lai, T. Basheer, V. L. Kuznetsov, R. G. Egdell, R. M. J. Jacobs, M. Pepper and P. P. Edwards, *J. Appl. Phys.*, 2012, **112**, 083708.
- 18 A. Janotti and C. G. Van de Walle, *Reports Prog. Phys.*, 2009, **72**, 6501.
- 19 P. Nunes, A. Malik, B. Fernandes, E. Fortunato, P. Vilarinho and R. Martins, *Vacuum*, 1999, **52**, 45–49.
- 20 M. Purica, *Thin Solid Films*, 2002, **403-404**, 485–488.
- 21 J. B. Franklin, B. Zou, P. Petrov, D. W. McComb, M. P. Ryan, M. A. McLachlan, J. B. Franklin, B. Zou, D. W. McComb, P. Petrov, M. P. Ryan and M. A. McLachlan, *J. Mater. Chem.*, 2011, **21**, 8178–8182.
- 22 K. H. Kim, K. C. Park and D. Y. Ma, *J. Appl. Phys.*, 1997, **81**, 7764.
- 23 S. Chen, N. Noor, I. P. Parkin and R. Binions, *J. Mater. Chem. A*, 2014, **2**, 17174–17182.
- 24 S. Chen, G. Carraro, D. Barreca, A. Sapelkin, W. Chen, X. Huang, Q. Cheng, F. Zhang and R. Binions, *J. Mater. Chem. A*, 2015, **3**, 13039–13049.
- 25 S. Chen, M. McLachlan, A. Sapelkin and R. Binions, *J. Mater. Chem. A*, 2015, **3**, 22311–22315.
- 26 J. B. Franklin, L. R. Fleet, C. H. Burgess and M. A. McLachlan, *Thin Solid Films*, 2014, **570**, Part , 129–133.
- 27 J. B. Franklin, J. M. Downing, F. Giuliani, M. P. Ryan and M. A. McLachlan, *Adv. Energy Mater.*, 2012, **2**, 528–531.
- 28 L. Krishnan Jagadamma, M. Abdelsamie, A. El Labban, E. Aresu, G. O. Ngongang Ndjawa, D. H. Anjum, D. Cha, P. Beaujuge and A. Amassian, *J. Mater. Chem. A*, 2014, **2**, 13321–13331.
- 29 A. Facchetti and T. J. Marks, *Transparent Electronics*, John Wiley & Sons, Ltd, Chichester, UK, 2010.
- 30 J. Zhang, J. C. D. Faria, M. Morbidoni, Y. Porte, C. H. Burgess, K. Harrabi and M. A. McLachlan, *Adv.*

- Electron. Mater.*, 2016.
- 31 J. C. D. Faria, A. J. Campbell and M. A. McLachlan, *Adv. Funct. Mater.*, 2015, **25**, 4657–4663.
- 32 H. Faber, Y.-H. Lin, S. R. Thomas, K. Zhao, N. Pliatsikas, M. A. McLachlan, A. Amassian, P. A. Patsalas and T. D. Anthopoulos, *ACS Appl. Mater. Interfaces*, 2015, **7**, 782–90.
- 33 G. Adamopolous, S. Thomas, P. Wokenberg, D. D. C. Bradley, M. A. McLachlan and T. D. Anthopoulos, *Adv. Mater.*, 2011, **23**, 1894–1898.
- 34 S. A. Studenikin, N. Golego and M. Cocivera, *J. Appl. Phys.*, 1998, **83**, 2104.
- 35 J. De Merchant and M. Cocivera, *Chem. Mater.*, 1995, **7**, 1742–1749.
- 36 H. Faber, B. Butz, C. Dieker, E. Spiecker and M. Halik, *Adv. Funct. Mater.*, 2013, **23**, 2828–2834.
- 37 Y. H. Lin, H. Faber, K. Zhao, Q. Wang, A. Amassian, M. A. McLachlan, T. D. Anthopoulos, Y.-H. Liu, H. Faber, K. Zhao, Q. Wang, A. Amassian, M. A. McLachlan and T. D. Anthopoulos, *Adv. Mater.*, 2013, **25**, 4340–4346.
- 38 R. Pandey, S. Yuldashev, H. D. Nguyen, H. C. Jeon and T. W. Kang, *Curr. Appl. Phys.*, 2012, **12**, S56–S58.
- 39 S.-W. Seo, S. H. Won, H. Chae and S. M. Cho, *Korean J. Chem. Eng.*, 2012, **29**, 525–528.
- 40 S. Gledhill, A. Grimm, D. Greiner, W. Bohne, M. Lux-Steiner and C.-H. Fischer, *Thin Solid Films*, 2011, **519**, 4293–4298.
- 41 R. C. Weast, .
- 42 K. F. Huang, T. M. Uen, Y. S. Gou, C. R. Huang and H. C. Yang, *Thin Solid Films*, 1987, **148**, 7–15.
- 43 D. H. Zhang and H. L. Ma, *Appl. Phys. A Mater. Sci. Process.*, 1996, **62**, 487–492.
- 44 K. Shirouzu, T. Kawamoto, N. Enomoto and J. Hojo, *Jpn. J. Appl. Phys.*, 2010, **49**, 010201 – 010203.
- 45 E. Hendry, M. Koeberg, J. Pijpers and M. Bonn, *Phys. Rev. B*, 2007, **75**, 233202.
- 46 Y. Wu, P. M. Hermkens, B. W. H. van de Loo, H. C. M. Knoop, S. E. Potts, M. A. Verheijen, F. Roozeboom and W. M. M. Kessels, *J. Appl. Phys.*, 2013, **114**, 024308.
- 47 S.-M. Park, T. Ikegami, K. Ebihara and P.-K. Shin, *Appl. Surf. Sci.*, 2006, **253**, 1522–1527.
- 48 K. U. Sim, S. W. Shin, a. V. Moholkar, J. H. Yun, J. H. Moon and J. H. Kim, *Curr. Appl. Phys.*, 2010, **10**, S463–S467.
- 49 J. Jia, A. Takasaki, N. Oka and Y. Shigesato, *J. Appl. Phys.*, 2012, **112**, 013718.
- 50 J. E. Stehr, K. M. Johansen, T. S. Bjørheim, L. Vines, B. G. Svensson, W. M. Chen and I. A. Buyanova, *Phys. Rev. Appl.*, 2014, **2**, 021001.
- 51 H. Hung-Chun Lai, T. Basheer, V. L. Kuznetsov, R. G. Egdell, R. M. J. Jacobs, M. Pepper and P. P. Edwards, *J. Appl. Phys.*, 2012, **112**.
- 52 a. El Manouni, F. J. Manjón, M. Mollar, B. Marí, R. Gómez, M. C. López and J. R. Ramos-Barrado, *Superlattices Microstruct.*, 2006, **39**, 185–192.
- 53 P. Arnou, J. W. Bowers and J. M. Walls, 2014, 308–313.
- 54 J.-H. Lee and B.-O. Park, *Mater. Sci. Eng. B*, 2004, **106**, 242–245.
- 55 M. T. Mohammad, a. a. Hashim and M. H. Al-Maamory, *Mater. Chem. Phys.*, 2006, **99**, 382–387.
- 56 M. de la L. Olvera, H. Gomez, A. Maldonado, H. Gómez and A. Maldonado, *Sol. Energy Mater. Sol. Cells*, 2007, **91**, 1449–1453.
- 57 S. Tewari and A. Bhattacharjee, 2011, **76**, 153–163.
- 58 G. Kenanakis, N. Katsarakis and E. Koudoumas, *Thin Solid Films*, 2014, **555**, 62–67.
- 59 Z. Ben Achour, T. Ktari, B. Ouertani, O. Touayar, B. Bessais and J. Ben Brahim, *Sensors Actuators A Phys.*, 2007, **134**, 447–451.
- 60 J. De Merchant and M. Cocivera, *Chem. Mater.*, 1995, 1742–1749.

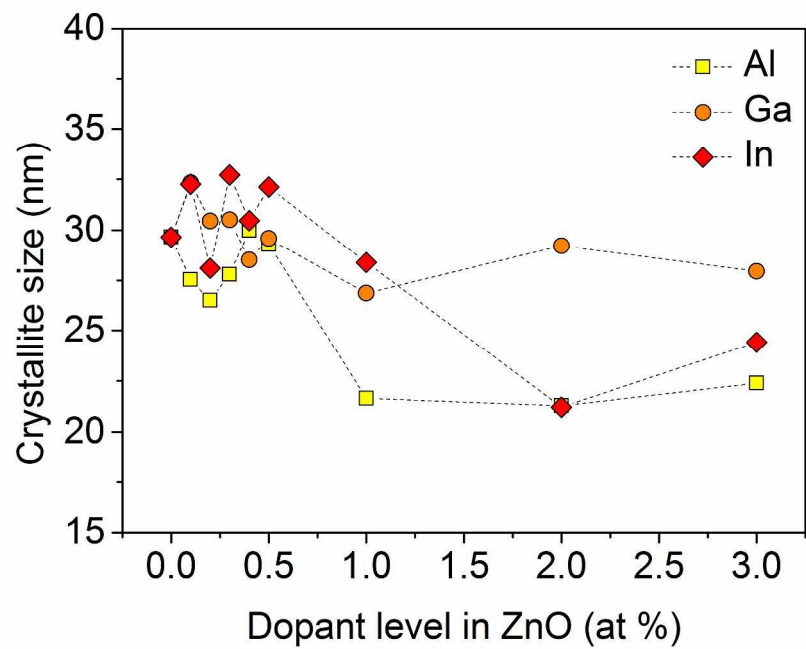
- 61 T. Y. Ma and S. C. Lee, *J. Mater. Sci. Mater. Electron.*, 2000, **1**, 305–309.
- 62 H. Gómez-Pozos, a. Maldonado and M. D. L. L. Olvera, *Mater. Lett.*, 2007, **61**, 1460–1464.
- 63 B. J. Babu, A. Maldonado, S. Velumani and D. D. I. Eléctrica-sees, .
- 64 B. J. Babu, a. Maldonado, S. Velumani and R. Asomoza, *Mater. Sci. Eng. B*, 2010, **174**, 31–37.
- 65 N. Jabena Begum and K. Ravichandran, *J. Phys. Chem. Solids*, 2013, **74**, 841–848.
- 66 E. Arca, K. Fleischer and I. Shvets, *Thin Solid Films*, 2014, **555**, 9–12.
- 67 F. A. Garcés, N. Budini, R. D. Arce and J. A. Schmidt, *Thin Solid Films*, 2015, **574**, 162–168.
- 68 R. Pandey, S. Yuldashev, H. D. Nguyen, H. C. Jeon and T. W. Kang, *Curr. Appl. Phys.*, 2012, **12**, S56–S58.
- 69 M. Soliman Selim, M. Chandra Sekhar and a. R. Raju, *Appl. Phys. A Mater. Sci. Process.*, 2004, **78**, 1215–1218.
- 70 A. F. Aktaruzzaman, G. L. Sharma and L. K. Malhotra, *Thin Solid Films*, 1991, **198**, 67–74.



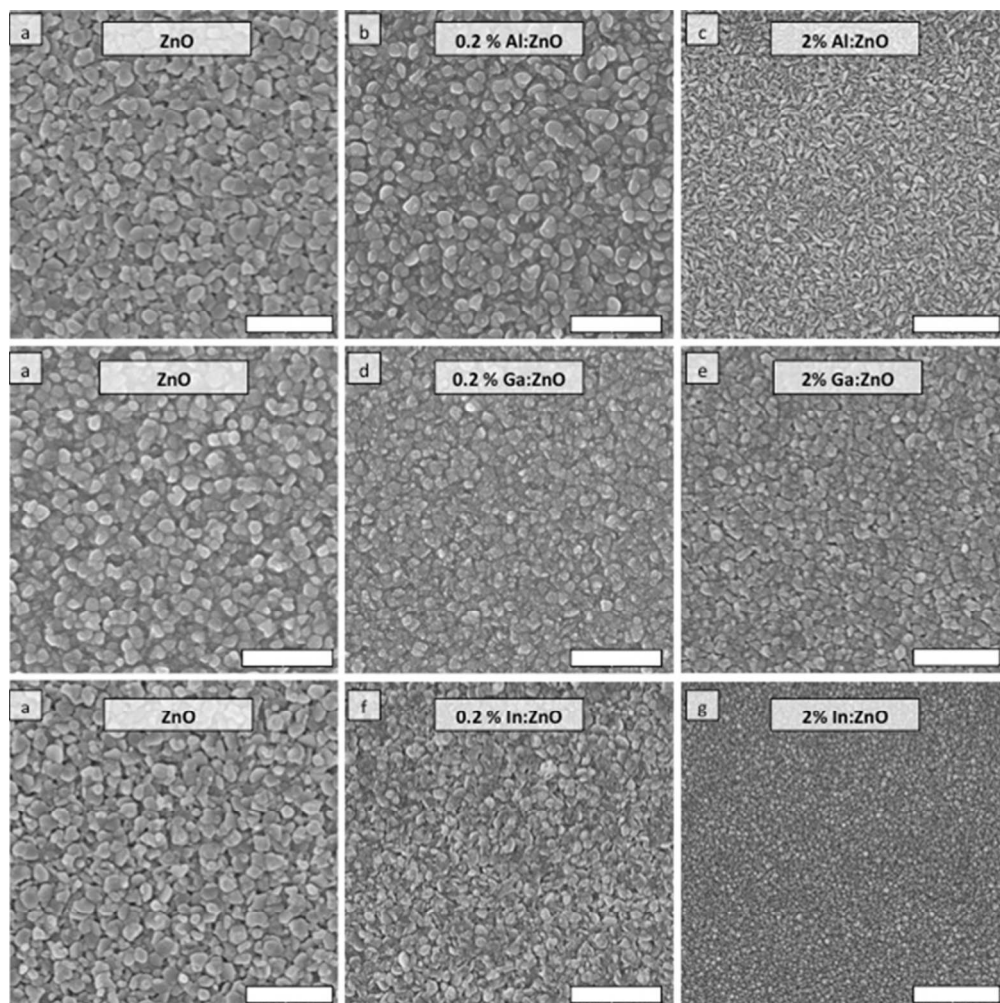
508x201mm (96 x 96 DPI)



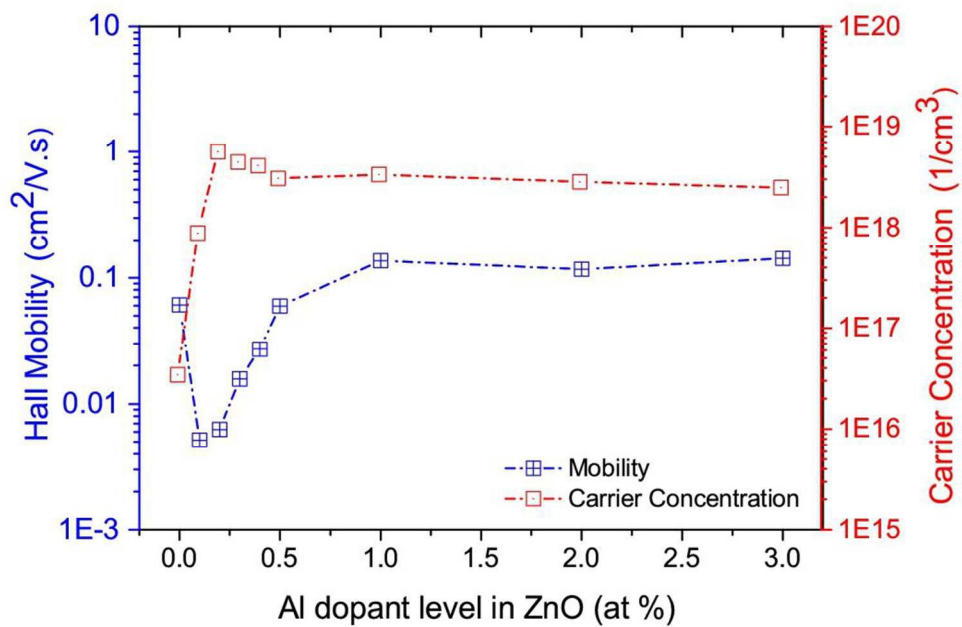
201x140mm (300 x 300 DPI)



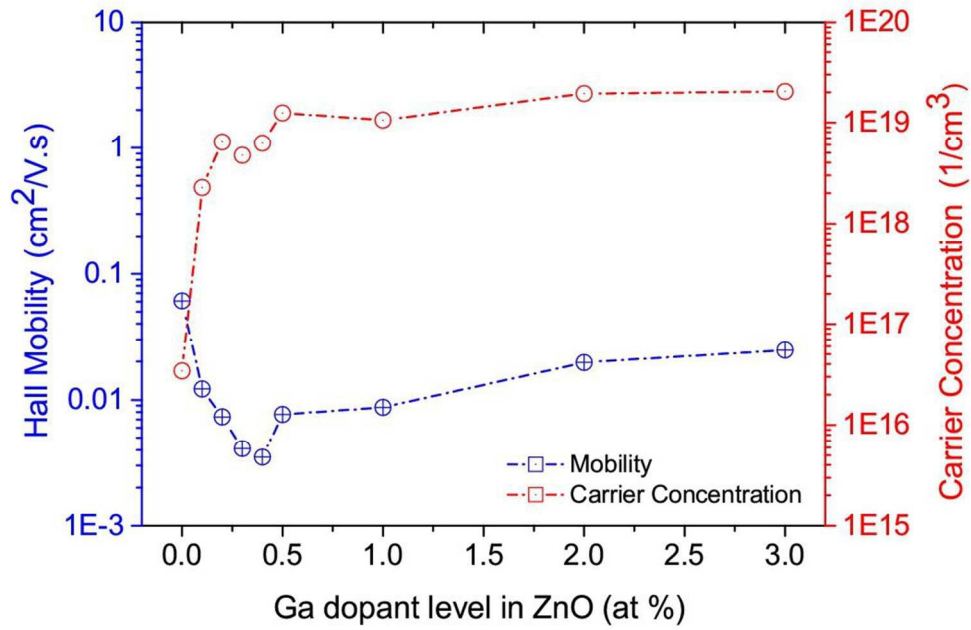
287x201mm (300 x 300 DPI)



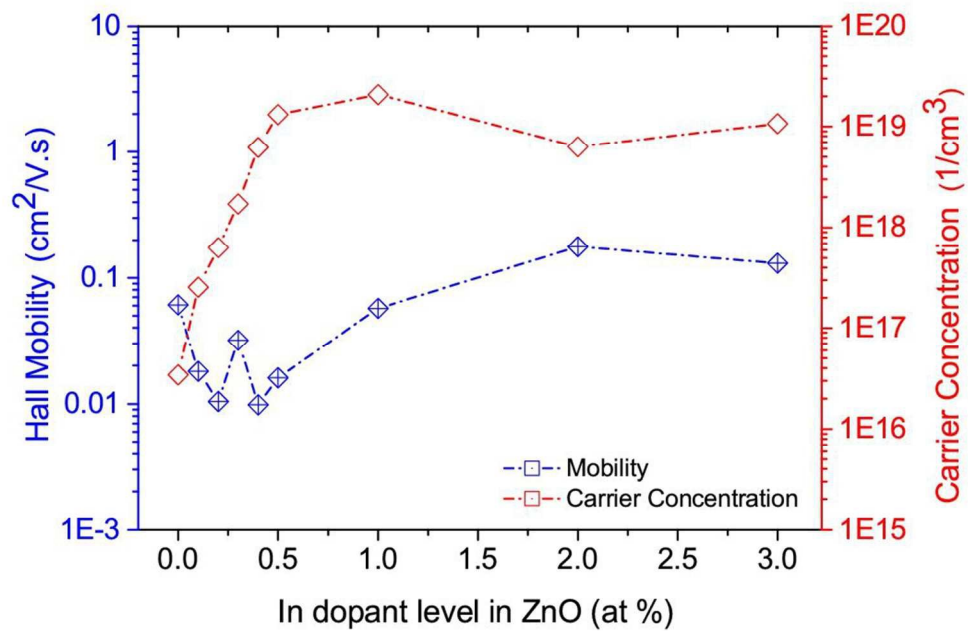
181x181mm (96 x 96 DPI)



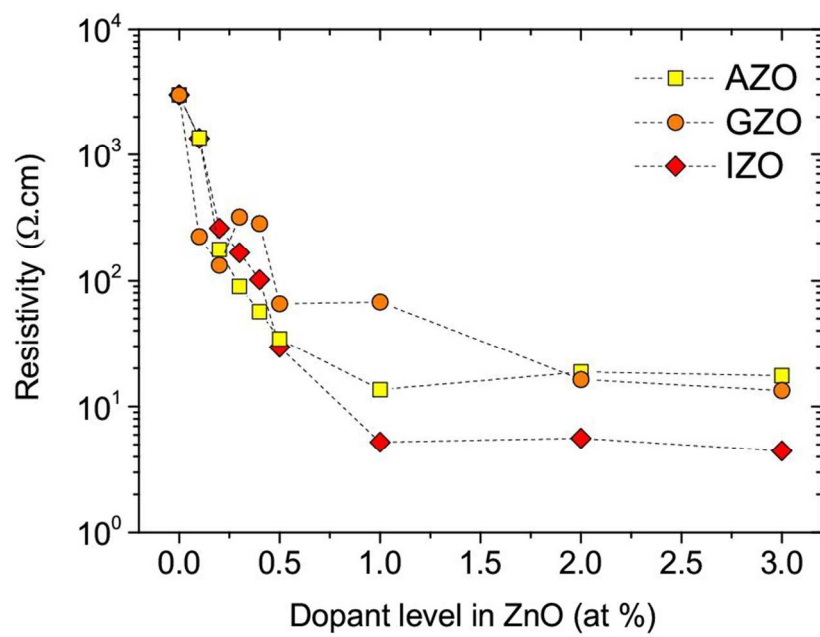
287x201mm (96 x 96 DPI)



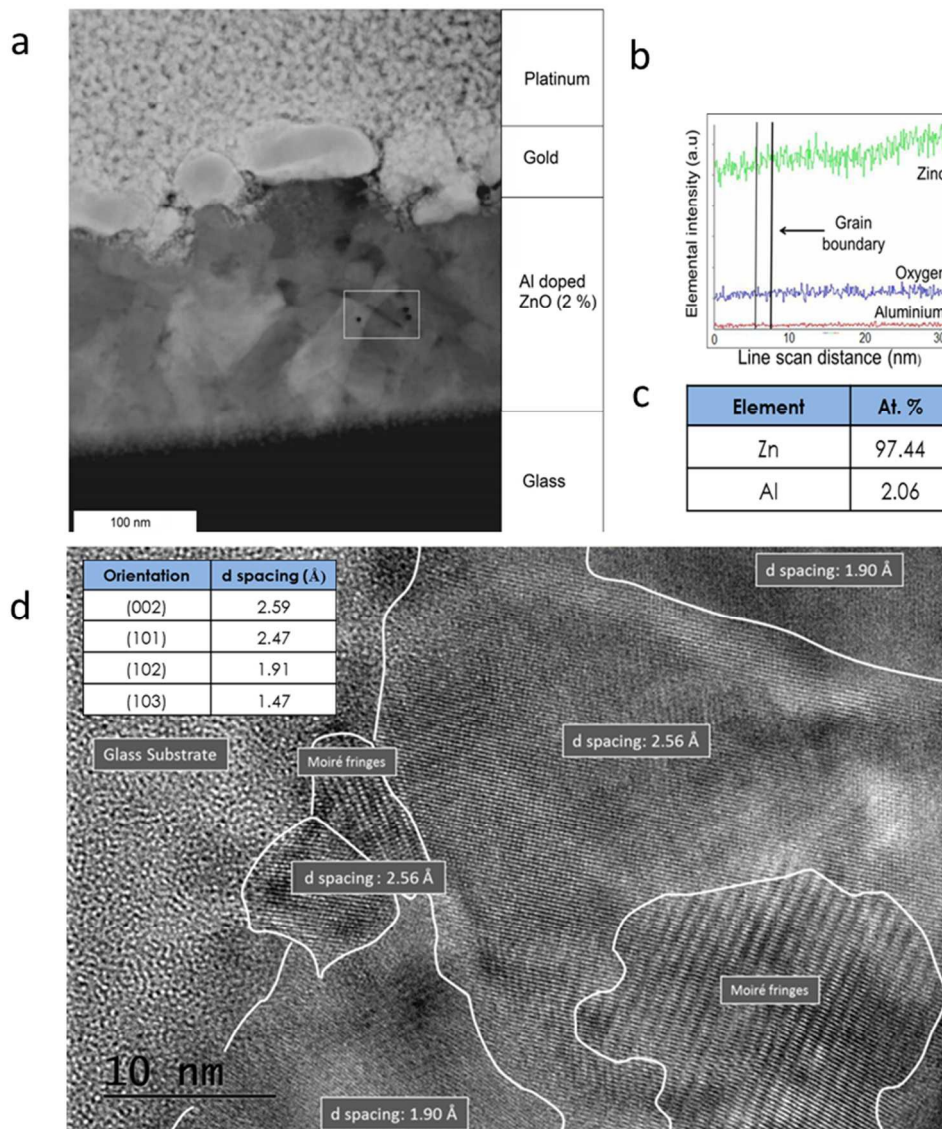
287x201mm (96 x 96 DPI)



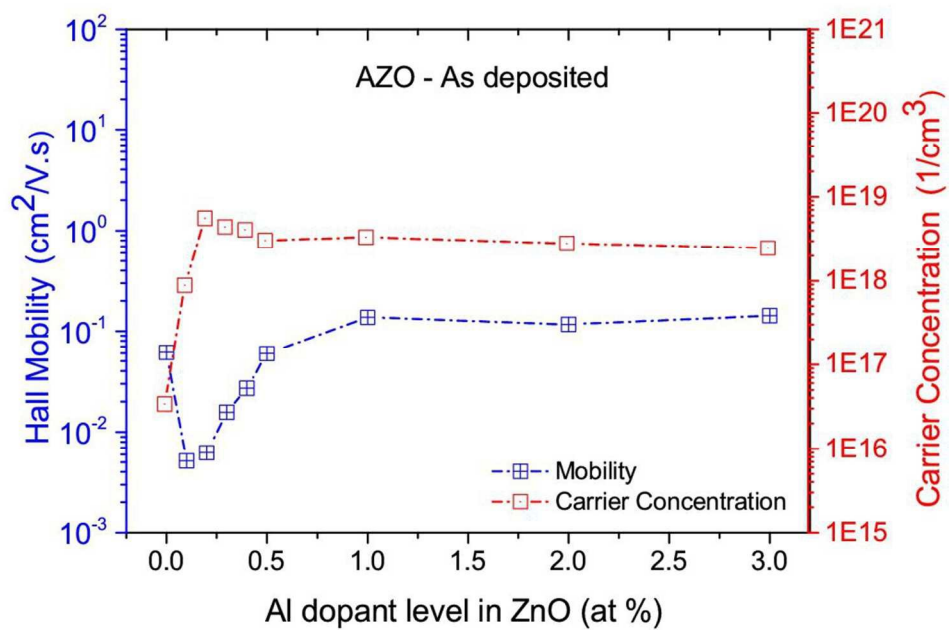
287x201mm (96 x 96 DPI)



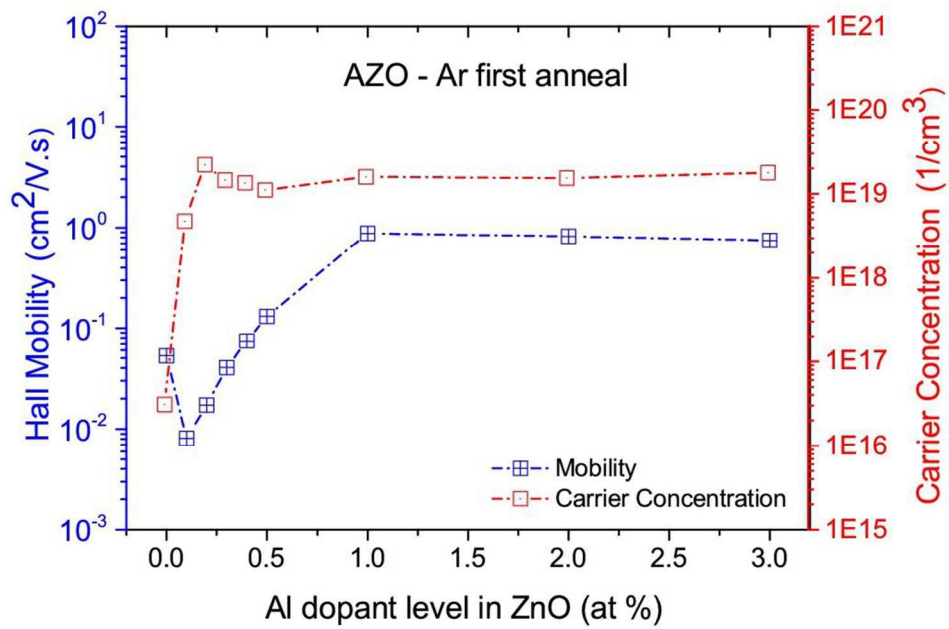
287x201mm (96 x 96 DPI)



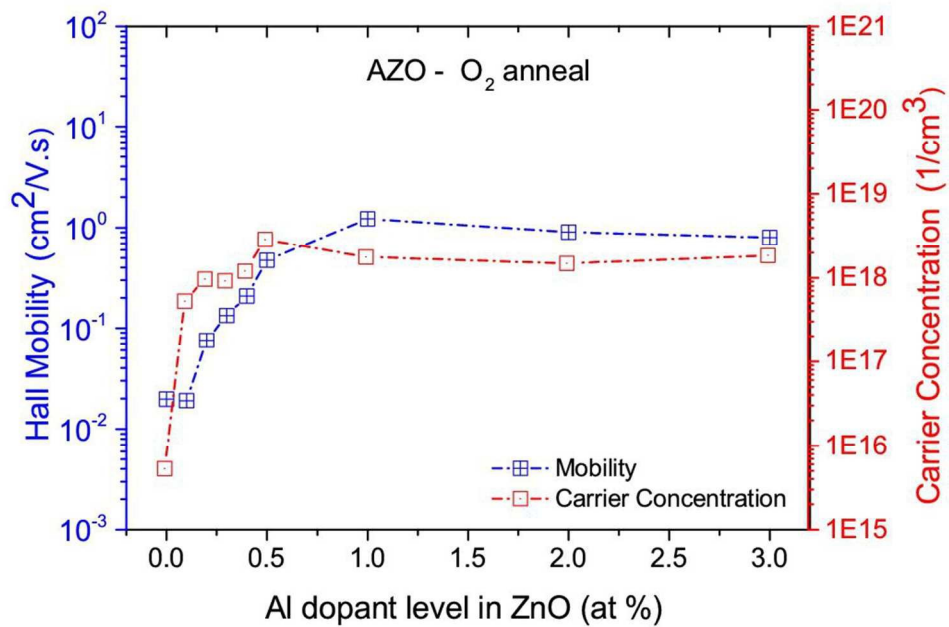
230x261mm (96 x 96 DPI)



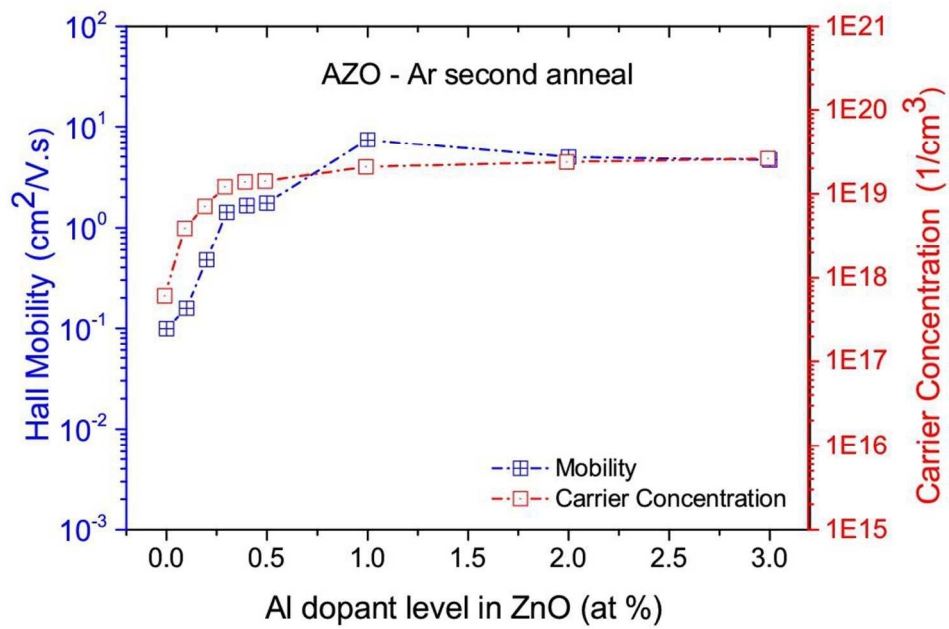
287x201mm (96 x 96 DPI)



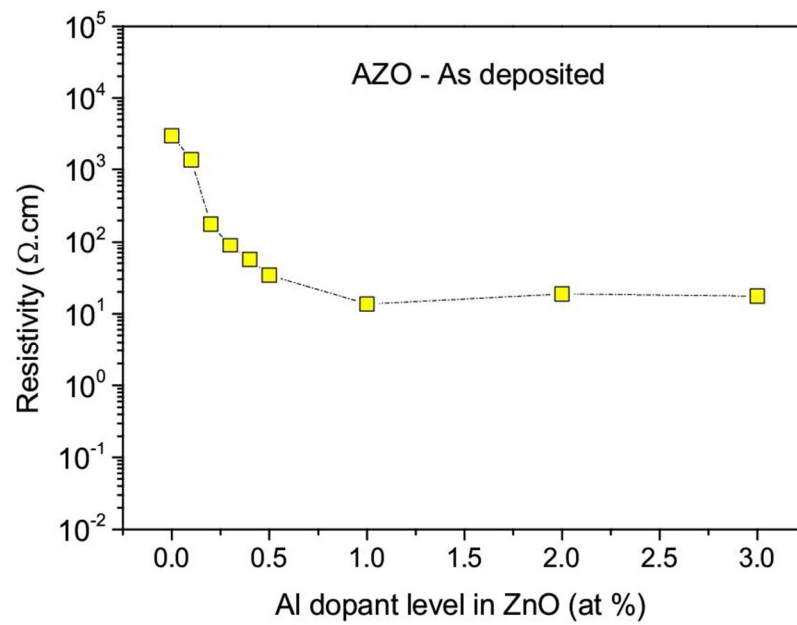
287x201mm (96 x 96 DPI)



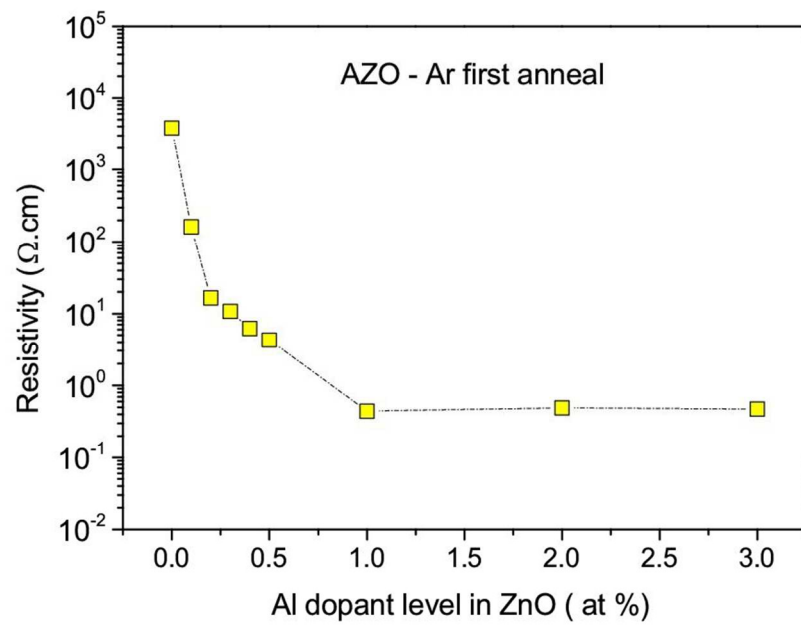
287x201mm (96 x 96 DPI)



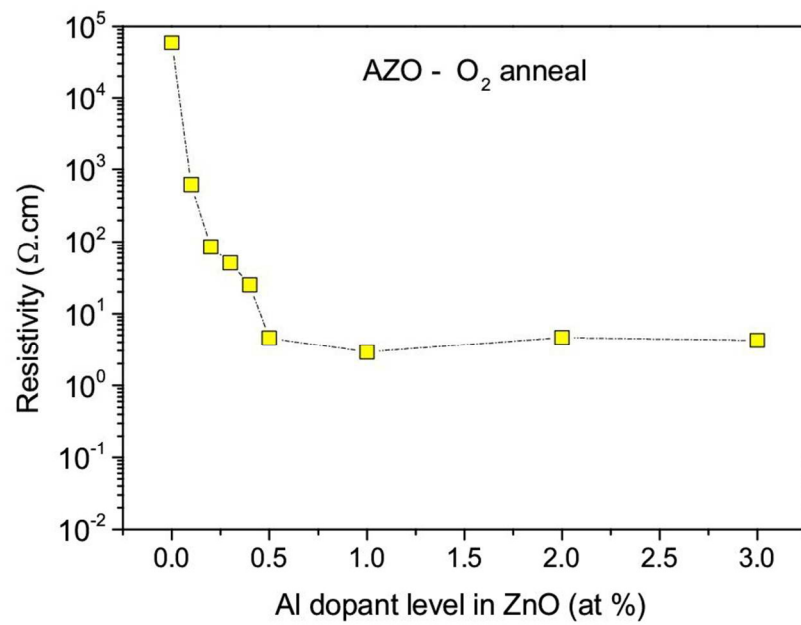
287x201mm (96 x 96 DPI)



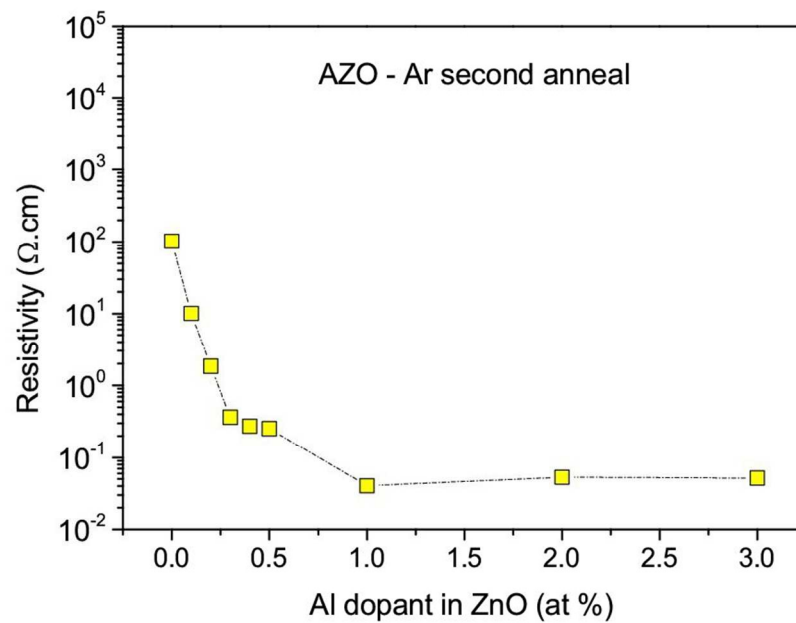
287x201mm (96 x 96 DPI)



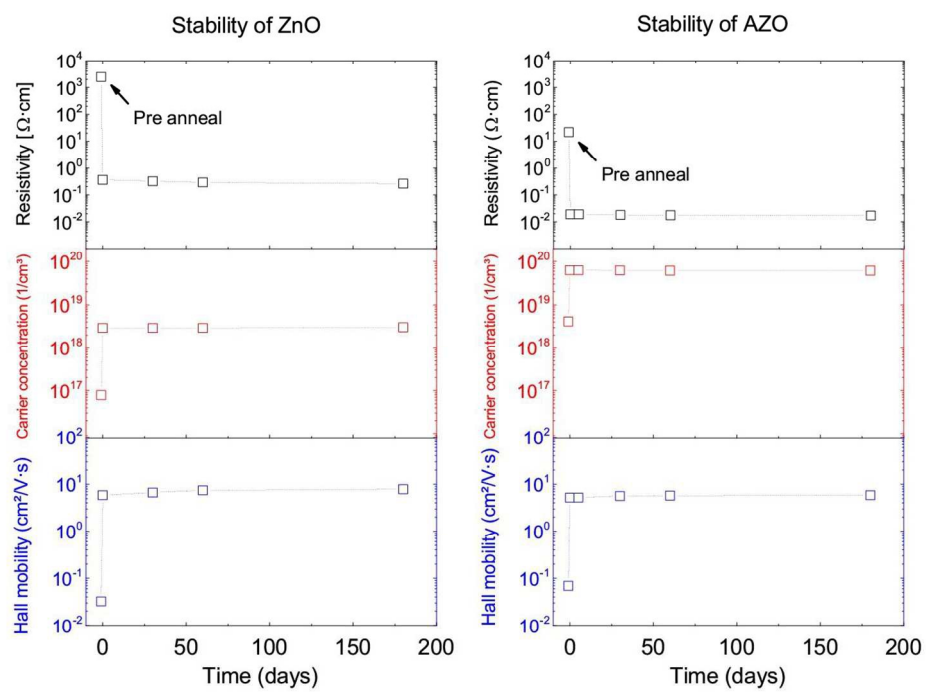
287x201mm (96 x 96 DPI)



287x201mm (96 x 96 DPI)



287x201mm (96 x 96 DPI)



381x287mm (96 x 96 DPI)